International Journal on Magnetic Particle Imaging
Vol 3, No 2, Article ID 1706005, 14 Pages

Infinite Science Publishing

Research Article

A Trajectory Study for Obtaining MPI System Matrices in a Compressed-Sensing Framework

Marco Maass[a,*] · Mandy Ahlborg[b] · Anna Bakenecker[b] · Fabrice Katzberg[a] · Huy Phan[a] · Thorsten M. Buzug[b] · Alfred Mertins[a]

[a] Institute for Signal Processing, University of Lübeck, Lübeck, Germany
[b] Institute of Medical Engineering, University of Lübeck, Lübeck, Germany
*Corresponding author, email: maass@isip.uni-luebeck.de

Received 25 November 2016; Accepted 1 May 2017; Published online 22 June 2017

Abstract

In this paper, we study the efficiency of five different field free point trajectories in two-dimensional magnetic particle imaging for the compressed-sensing based reconstruction of partially measured system matrices. To show the suitability of the trajectories, different trajectories with identical repetition times were simulated using the same scanner setup. We show that for all trajectories, the compressed-sensing based reconstruction approach for the system matrix is possible and promising for real-world scenarios. Also we validate the already known fact that the Lissajous trajectory is appropriate for the compressed sensing approach. Furthermore, the results show that there are still other trajectory choices which show similar and even better performance in the compressed-sensing based reconstruction.

I. Introduction

Magnetic particle imaging is a tracer-based imaging method which can visualize the spatial distribution of super-paramagnetic iron oxid nanoparticels (SPIONs) [1]. To image the SPIONs' distribution within a field of view (FOV) commonly a field free point (FFP) is used. With the help of a static magnetic field, the so-called selection field, the FFP is generated. Only SPIONs in the vicinity of the FFP contribute significantly to the measured voltage signal, because SPIONs far away from the FFP are in saturation due to their nonlinear magnetization behavior. An additional dynamic drive field moves the FFP along a trajectory to image an area of interest. For reconstruction, a system matrix based method is widely used [2]. Even with unchanged scanner setup, different trajectories result in different system functions. For most trajectories, no closed-form solutions for the system function are known. Therefore, in general, system matrices need to be measured [2]. Unfortunately, the measurement of the system matrix with a robot can take several days for significant resolution inside the FOV. To address this problem, different approaches have been published. One method is the reconstruction without a system matrix directly in the time domain, called x-space reconstruction [3], but the x-space reconstruction is not easily transferable to every trajectory. Also, the reconstruction based on a measured system matrix allows better reconstruction of the particle distribution. A more recent method to measure the system matrix is based on magnetic-particle spectrometry. Here, magnetic fields of the scanner are emulated and the signal response near the particle probe is measured. The bene-

fits are a significantly higher signal-to-noise ratio (SNR) and a reduced acquisition time compared to the robot-based measurement. The resulting system matrix is also known as hybrid system matrix in the literature [4, 5]. Following the idea of compressed sensing (CS) [6], in [7] a method for a partially measured system matrix based on a Lissajous trajectory was introduced. Several symmetry conditions for Lissajous trajectory based MPI system matrices have been presented [8], and, additionally, a method which combines the symmetry condition with the compressed sensing based approach was introduced [9]. To the best of the authors' knowledge, no systematical study of the capability of different trajectories in the context of CS-based system matrix reconstruction has been carried out so far. In this paper, we demonstrate in a simulation study based on system matrices from an MPI scanner with five different FFP trajectories that all trajectories are appropriate for CS-based reconstruction. With two different phantoms we demonstrate the capability of the CS-based system matrices to reconstruct the particle distribution.

II. MPI system function

The relationship between the induced voltage signal $u_\ell(t)$ in the ℓ-th receive channel and the particle concentration $c(\boldsymbol{r})$ is commonly described by the Fourier series expansion coefficients

$$\hat{u}_{\ell,k} = \int_\Omega \hat{s}_{\ell,k}(\boldsymbol{r}) c(\boldsymbol{r}) d\boldsymbol{r}, \tag{1}$$

where $\hat{s}_{\ell,k}(\boldsymbol{r})$ is the k-th system function component of the ℓ-th receive channel, and $\Omega \subset \mathbb{R}^d$ denotes the FOV of dimensionality d. The system function component in (1) is described by

$$\hat{s}_{\ell,k}(\boldsymbol{r}) = -\hat{a}_{\ell,k} \frac{\mu_0}{T} \int_{t_0}^{t_0+T} \frac{\partial}{\partial t} \left(\overline{\boldsymbol{m}}(\boldsymbol{r},t) \cdot \boldsymbol{p}_\ell(\boldsymbol{r}) \right) e^{-2\pi \mathrm{i} \frac{kt}{T}} dt, \tag{2}$$

where $\hat{a}_{\ell,k}$ denotes the transfer function of the ℓ-th receive chain, μ_0 is the vacuum permeability, T is the repetition time of the acceleration field, $t_0 \in \mathbb{R}$ is an arbitrary time offset, $\overline{\boldsymbol{m}}(\boldsymbol{r},t)$ describes the mean magnetic moment, and $\boldsymbol{p}_\ell(\boldsymbol{r})$ denotes the coil-sensitivity profiles. In a first simplified physical model for isotropic SPIONs with instantaneous relaxation, the relationship between the applied magnetic field $\boldsymbol{H}(\boldsymbol{r},t)$ of the scanner and the mean magnetic moment $\overline{\boldsymbol{m}}(\boldsymbol{r},t)$ is given by

$$\overline{\boldsymbol{m}}(\boldsymbol{r},t) = \overline{m}(\|\boldsymbol{H}(\boldsymbol{r},t)\|) \frac{\boldsymbol{H}(\boldsymbol{r},t)}{\|\boldsymbol{H}(\boldsymbol{r},t)\|}, \tag{3}$$

with $\|\cdot\|$ the euclidean norm and $\overline{m}(H)$ the magnitude of the mean magnetic moment, which is proportional to the Langevin function [2]. The applied magnetic field

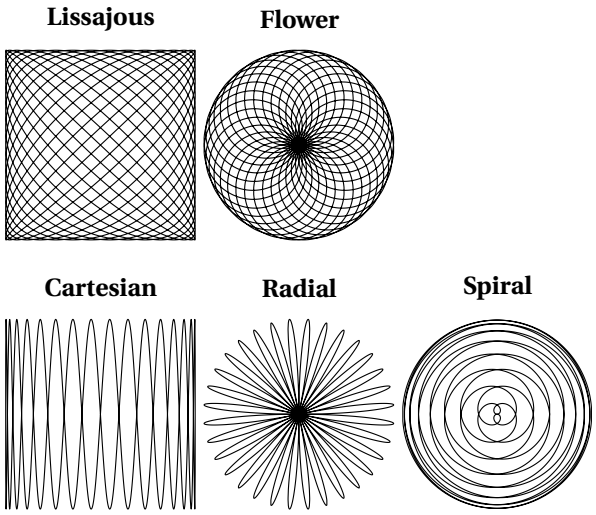

Figure 1: The five different trajectories for $N_B = 16$.

$\boldsymbol{H}(\boldsymbol{r},t)$ of the MPI scanner is given by a superposition $\boldsymbol{H}(\boldsymbol{r},t) = \boldsymbol{H}^S(\boldsymbol{r}) + \boldsymbol{H}^D(t)$ of the so-called selection field $\boldsymbol{H}^S(\boldsymbol{r})$ and drive field $\boldsymbol{H}^D(t)$, which perform the spatial and temporal encoding, respectively. For the two-dimensional imaging process ($d = 2$), the selection field is given by

$$\boldsymbol{H}^S(\boldsymbol{r}) = \boldsymbol{G}\boldsymbol{r} \quad \text{with} \quad \boldsymbol{G} = \begin{pmatrix} G_1 & 0 \\ 0 & G_2 \end{pmatrix}. \tag{4}$$

The temporal encoding by the drive field

$$\boldsymbol{H}^D(t) = \begin{pmatrix} H_1^D(t) \\ H_2^D(t) \end{pmatrix} \tag{5}$$

can be performed using different periodic trajectories. In Tab. 1 the drive fields simulated in this work are introduced, in the following referred to as trajectories. To produce the different behavior, two different excitation frequencies $f_1 = \omega_1/(2\pi)$ and $f_2 = \omega_2/(2\pi)$ are calculated according to the rules shown in Tab. 1, with $f_1 = f_B/N_B$, f_B being a chosen basis frequency and $N_B \in \mathbb{N}$. The repetition time for all trajectories in Tab. 1 is $T = N_B(N_B-1)/f_B$. All drive fields $\boldsymbol{H}^D(t)$ are simple combinations of sine and cosine functions and can easily be realized in hardware. In Fig. 1, the resulting trajectories are shown for $N_B = 16$.

III. The system matrix

An important issue in MPI is the lack of a closed-form solution for the system function in more than one dimension. In one-dimensional MPI with the simplified model, as defined in the previous section, the system function components are related to the Chebyshev polynomials of second-kind [11]. However, for two- and three-dimensional MPI, to this point, no closed-form solution

Table 1: An overview of different two-dimensional drive fields $\boldsymbol{H}^D(t)$ and the required frequency-ratios, where $\omega_i = 2\pi f_i$. The table was obtained from [10].

Frequency-ratio	Trajectory	Drive field $\boldsymbol{H}^D(t)$
$\omega_1 = \frac{N_B-1}{N_B}\omega_2$	**Lissajous**	$\begin{pmatrix} A_1\sin(\omega_1 t) \\ A_2\sin(\omega_2 t)\end{pmatrix}$
	Flower	$\begin{pmatrix} A_1\sin(\omega_1 t)\cos(\omega_2 t) \\ A_2\sin(\omega_2 t)\sin(\omega_1 t)\end{pmatrix}$
$\omega_2 = \frac{\omega_1}{N_B-1}$	**Cartesian**	$\begin{pmatrix} A_1\sin(\omega_1 t) \\ A_2\sin(\omega_2 t)\end{pmatrix}$
	Radial	$\begin{pmatrix} A_1\sin(\omega_1 t)\cos(\omega_2 t) \\ A_2\sin(\omega_2 t)\sin(\omega_1 t)\end{pmatrix}$
	Spiral	$\begin{pmatrix} A_1\sin(\omega_1 t)\sin(\omega_2 t) \\ A_2\sin(\omega_2 t)\cos(\omega_1 t)\end{pmatrix}$

has been derived and the simplified physical model excluding the relaxation effects of the particles causes additional problems for complex trajectories. Therefore, the system matrix is normally measured for each scanner in an initial calibration step with a point-like sample, which results in a spatial discretization of the form

$$\begin{aligned} r_1^u &= \frac{A_1}{G_1} - \frac{A_1}{N_1 G_1}(1+2u) \quad \text{and} \\ r_2^v &= \frac{A_2}{G_2} - \frac{A_2}{N_2 G_2}(1+2v), \end{aligned} \tag{6}$$

where $u \in \{0,1,\dots,N_1-1\}$ and $v \in \{0,1,\dots,N_2-1\}$ describe the equidistant spatial sampling of $\boldsymbol{r}$ inside the FOV in two dimensions. The discrete version $\hat{s}_{\ell,k}(r_1^u, r_2^v)$ is, for convenience, denoted by the discrete indices u and v as $\hat{s}_{\ell,k}(u,v)$. During our simulations, the integral in (1) has been numerically approximated with help of the midpoint quadrature rule. In real-world measurements, the voltage signal $u_\ell(t)$ will be sampled, but if the Shannon-Nyquist sampling theorem is fulfilled, the Fourier coefficients $\hat{u}_{\ell,k}$ can be calculated from the sampled periodic signal $u_\ell(t_n)$ by using the discrete Fourier transform (DFT), where

$$t_n = \frac{nT}{N_t} \quad (n \in [0,\dots,N_t-1]) \tag{7}$$

denotes the sampled time points, T is the repetition time of the trajectory, and $N_t \in \mathbb{N}$ is the number of sampling points. We finally have in total $2K-1$ different frequency components, where $K < \frac{N_t}{2}$ and $K \in \mathbb{N}$. The existing discrete system function components $\hat{s}_{\ell,k}(u,v)$ with $k \in \{-K+1,\dots,0,\dots,K-1\}$ can then be reordered in the system matrix

$$\hat{\boldsymbol{S}}_\ell = \Delta V \begin{pmatrix} \hat{s}_{\ell,0}(\varphi_0) & \hat{s}_{\ell,0}(\varphi_1) & \dots & \hat{s}_{\ell,0}(\varphi_{N_1N_2-1}) \\ \hat{s}_{\ell,1}(\varphi_0) & \hat{s}_{\ell,1}(\varphi_1) & \dots & \hat{s}_{\ell,1}(\varphi_{N_1N_2-1}) \\ \vdots & \vdots & \ddots & \vdots \\ \hat{s}_{\ell,K-1}(\varphi_0) & \hat{s}_{\ell,K-1}(\varphi_1) & \dots & \hat{s}_{\ell,K-1}(\varphi_{N_1N_2-1}) \end{pmatrix}, \tag{8}$$

where φ_i denotes a bijective map on the coordinates of the spatial grid and ΔV denotes the volume of the voxels. Because the measured signals are real-valued, the negative frequency components are only complex conjugates of the positive ones, so that they can be excluded from $\hat{\boldsymbol{S}}_\ell \in \mathbb{C}^{K \times N_1 \cdot N_2}$. For the sake of clarity, we omit the voxel volume ΔV throughout the following.

IV. System Matrix Compression

In [12] it was observed that MPI system matrices for an MPI scanner using an FFP moving along a Lissajous-trajectory are highly compressible. The focus in [12] was to speed up the reconstruction process by using orthogonal transforms to compress the system matrices and to reduce memory usage during the image reconstruction. In [12], it was mentioned that the discrete cosine transform of second-kind (DCT-II) and the discrete Chebyshev transform (DTT) showed good compression behavior for the spatial domain of the system function components in the system matrix. Additionally, several symmetry conditions on the system function component $\hat{s}_{\ell,k}(\boldsymbol{r})$ could be shown [8] that should be preserved by any compressive orthogonal transform [8, 13]. Because the DCT-II fulfills this symmetry conditions for an MPI scanner using a FFP moving along a Lissajous-trajectory and since it is an orthogonal transform that can be efficiently computed, it will be used in the following.

The compression of the system matrix of the ℓ-th receive channel is carried out in the form

$$\tilde{\boldsymbol{S}}_\ell = \hat{\boldsymbol{S}}_\ell \boldsymbol{T}^T, \tag{9}$$

where $\boldsymbol{T} \in \mathbb{R}^{N_1 \cdot N_2 \times N_1 \cdot N_2}$ is an orthogonal matrix. To enforce zeros inside the compressed system matrix $\tilde{\boldsymbol{S}}_\ell$, Lampe et al. [12] compared the magnitudes of the coefficients in $\tilde{\boldsymbol{S}}_\ell$ to a global threshold and set coefficients with a magnitude smaller than the global threshold to zero. Alternatively, in [14] a local thresholding strategy was proposed. Here, for each compressed system function component $\tilde{s}_{\ell,k}(u,v)$, a fixed number of values was selected based on their magnitudes, and the rest of the coefficients was set to zero. In [14] and [13] it was shown that the local thresholding strategy outperforms the global one.

V. Compressed Sensing

Compressed Sensing is a method which uses the compressibility of a signal in a sparsity domain to reconstruct the signal in the original domain, where the Nyquist-Shannon sampling theorem is not directly fulfilled [6]. The rough idea can be explained by the underdetermined reconstruction problem

$$\arg\min_{\boldsymbol{x}} \|\boldsymbol{x}\|_0 \quad \text{s.t.} \quad \boldsymbol{y} = \boldsymbol{A}\boldsymbol{x}, \tag{10}$$

where $\boldsymbol{A} = \boldsymbol{\Phi}\boldsymbol{\Psi} \in \mathbb{R}^{M\times N}$ with $M \ll N$ contains the measurement matrix $\boldsymbol{\Phi} \in \mathbb{R}^{M\times N}$ and the sparsity basis $\boldsymbol{\Psi} \in \mathbb{R}^{N\times N}$, $\boldsymbol{y} \in \mathbb{R}^M$ the measurement vector, $\boldsymbol{x} \in \mathbb{R}^N$ is the sparse signal which is to be reconstructed, and $\|\cdot\|_0$ denotes the zero-pseudonorm counting the number of nonzero entries. The signal in the non-sparse domain is represented as $\boldsymbol{x}_{\boldsymbol{\Psi}} = \boldsymbol{\Psi}\boldsymbol{x}$. The drawback of the formulation in equation (10) is the NP-hardness, which means that under the hypothesis that NP≠P there is no deterministic polynomial-time algorithm to solve the problem exactly, so that in literature different methods have been established. One widely used possibility is to replace the non-convex ℓ_0-pseudonorm by the convex ℓ_1-norm. The formulation of the problem then becomes

$$\arg\min_{\boldsymbol{x}} \|\boldsymbol{x}\|_1 \quad \text{s.t.} \quad \boldsymbol{y} = \boldsymbol{A}\boldsymbol{x}. \tag{11}$$

To answer the question under which condition the convex problem in (11) is equivalent to the non-convex problem in (10), different measures were introduced. One famous definition is the so-called restricted isometry property (RIP) presented in [15]. However, the evaluation of the RIP for a given matrix $\boldsymbol{A}$ is as hard as the reconstruction problem (10) itself. Interestingly, for many classes of random matrices (e.g. Gaussian, Bernoulli, Rademacher, etc.) it can be shown that the RIP is fulfilled with high probability for a wide range of $M \ll N$. From a practical point of view, however, the RIP is not a good tool to evaluate the equivalence.

For a special group of matrices $\boldsymbol{A}$ a more tractable approach is based on the mutual coherence [16]

$$\mu(\boldsymbol{A}) = \max_{k,j\in\{0,1\ldots,N-1\}:k\neq j} \frac{\left|\langle \boldsymbol{a}_k, \boldsymbol{a}_j\rangle\right|}{\|\boldsymbol{a}_k\|\cdot\|\boldsymbol{a}_j\|}. \tag{12}$$

and the inequality

$$S < \frac{1}{2}\left(1 + \frac{1}{\mu(\boldsymbol{A})}\right), \tag{13}$$

where $S = \|\boldsymbol{x}^0\|_0$ is the number of non-zero entries in $\boldsymbol{x}^0 \in \mathbb{R}^N$. If the inequality (13) is satisfied, then $\boldsymbol{x}^0$ is the unique solution to the ℓ_0-problem (10) and can be found by solving the ℓ_1-problem (11) [17–19]. It becomes obvious in (13) that a perfect recovery can be guaranteed for a wide range of S if the mutual coherence $\mu(\boldsymbol{A}) = \mu(\boldsymbol{\Phi}\boldsymbol{\Psi})$ is low. Thus, in a practical measurement procedure, $\boldsymbol{\Phi}$ and $\boldsymbol{\Psi}$ should be selected together to ensure a small mutual coherence.

If white Gaussian noise $\boldsymbol{n} \in \mathbb{R}^M$ is expected in the measurement process $\boldsymbol{y} = \boldsymbol{A}\boldsymbol{x} + \boldsymbol{n}$, different relaxed convex optimization problems can be derived from (11). In this paper, the relaxation

$$\arg\min_{\boldsymbol{x}} \|\boldsymbol{A}\boldsymbol{x} - \boldsymbol{y}\|_2^2 + \lambda\|\boldsymbol{x}\|_1, \quad \text{with} \quad \lambda > 0 \tag{14}$$

is used. For the problem (14), different global optimal solvers exist in the literature [20–23].

V.I. Compressed Sensing based system matrix reconstruction

In [7] the compressibility of the system matrix was firstly used to reconstruct the system matrices from only partial measurements. In [9] the compressed sensing based method was extended by using the symmetry properties, which were shown in [8] for Lissajous-trajectory based MPI. The basic idea in [7] is to partially measure the FOV with point-samples. The partial measurement of the FOV can be expressed with an undersampling matrix $\boldsymbol{U} = (\boldsymbol{e}_i)_{i\in\mathscr{U}} \in \mathbb{R}^{N_1N_2\times M}$, where $\mathscr{U} \subset \{1,2,\ldots,N_1N_2\}$, $M = \#(\mathscr{U})$ is the cardinality of $\mathscr{U}$, and $\boldsymbol{e}_i \in \mathbb{R}^{N_1N_2}$ is the i-th unit vector. The sampled FOV points $\mathscr{U}$ are normally chosen as random subselection of all possible FOV points to enforce incoherence for the CS-based reconstruction of the system matrix. The sampling of the partially measured system matrix is then described by

$$\hat{\boldsymbol{S}}_\ell^p = \hat{\boldsymbol{S}}_\ell \boldsymbol{U}. \tag{15}$$

Now let $\boldsymbol{T} \in \mathbb{R}^{N_1N_2\times N_1N_2}$ denote an orthogonal compressive transform in the spatial domain (see Section IV), so that

$$\hat{\boldsymbol{S}}_\ell = \tilde{\boldsymbol{S}}_\ell \boldsymbol{T}^T, \tag{16}$$

where $\tilde{\boldsymbol{S}}_\ell$ is the compressed version of $\hat{\boldsymbol{S}}_\ell$.

The reconstruction problem in (14) is then solved for each system function component k and receive channel ℓ for the real parts

$$\tilde{\boldsymbol{s}}_{\ell,k}^{\mathrm{r}} = \left[\Re\left\{\tilde{s}_{\ell,k}(\varphi_0)\right\}, \ldots, \Re\left\{\tilde{s}_{\ell,k}(\varphi_{N_1N_2-1})\right\}\right]^T$$

and imaginary parts

$$\tilde{\boldsymbol{s}}_{\ell,k}^{\mathrm{i}} = \left[\Im\left\{\tilde{s}_{\ell,k}(\varphi_0)\right\}, \ldots, \Im\left\{\tilde{s}_{\ell,k}(\varphi_{N_1N_2-1})\right\}\right]^T$$

individually. Note that these are the real and imaginary parts of the rows of $\tilde{\boldsymbol{S}}_\ell$, turned into column vectors. For the optimization, the partial measurements vector also has to be split into real $\hat{\boldsymbol{s}}_{\ell,k}^{\mathrm{p,r}} = \left(\Re\left\{\hat{s}_{k,\ell}(\varphi_i)\right\}\right)_{i\in\mathscr{U}}$ and imaginary $\hat{\boldsymbol{s}}_{\ell,k}^{\mathrm{p,i}} = \left(\Im\left\{\hat{s}_{k,\ell}(\varphi_i)\right\}\right)_{i\in\mathscr{U}}$ parts. Hereby, the optimization problem in (14) is solved as

$$\tilde{\boldsymbol{s}}_{k,\ell}^t = \arg\min_{\boldsymbol{x}\in\mathbb{R}^{N_1N_2}} \|\boldsymbol{U}^T\boldsymbol{T}\boldsymbol{x} - \hat{\boldsymbol{s}}_{k,\ell}^{\mathrm{p},t}\|_2^2 + \lambda\|\boldsymbol{x}\|_1, \tag{17}$$

10.18416/ijmpi.2017.1706005

where $t \in \{\mathrm{r},\mathrm{i}\}$ denotes the real and imaginary parts, respectively, $\boldsymbol{\Phi} = \boldsymbol{U}^T$, $\boldsymbol{\Psi} = \boldsymbol{T}$, and $\boldsymbol{y} = \hat{\boldsymbol{s}}^{\mathrm{p},t}_{k,\ell}$. Therefore, it becomes recognizable that the random sampling pattern decoded in $\boldsymbol{U}$ should be optimized to enforce incoherence for a given $\boldsymbol{T}$ (2D DCT-II). Furthermore, the sampling pattern seems directly independent from the choice of the FFP trajectory for the MPI scanner, whereas it will be shown that the reconstruction error inside the system matrices for a given uniformly sampled spatial sampling pattern is region dependent. The optimization problem is then finally solved by the FISTA algorithm [23], which was also used in [7] and [9].

VI. Test setup

We simulated five different system matrices for the MPI-scanner based on the trajectories in Tab. 1. For each scanner, a system matrix in x- and y-receive-channel was simulated. The base frequency was chosen as $f_B = 2.5/3\,\mathrm{MHz}$. With $N_B = 33$ being selected as frequency divider, it follows that $f_1 = f_B/33$. The second frequency f_2 can then be calculated as described in Tab. 1. In this case, the frequency ratio for the Lissajous and flower trajectories is $f_1/f_2 = 32/33$. The repetition time for all trajectories is 1.27 ms. Currently, within one repetition, 1632 time-points are sampled, which corresponds to 1632 frequency components in Fourier space and a sampling frequency of 1.3 MHz. The FOV has a size of $5\times5\,\mathrm{cm}^2$ and is discretized into 250×250 pixels. The maximal gradient strengths of the selection field in x- and y-directions are $1.25\,\mathrm{Tm}^{-1}$. The particle diameter is 30 nm, and the upper noise resistance in a patient is $0.185\,\mathrm{m}\Omega$ according to [24]. The resulting noise is included in the simulated system matrix and voltage signal, respectively. The particle temperature was chosen as the body temperature in a patient. The voltage signals for the phantoms were calculated on a finer 300×300 grid related to the simulated system matrices in this work.

To simulate the partial sampling of the grid, we performed a uniform random permutation of all possible grid indices. The random undersampling is then achieved by systematically using only the first given indices in the permutation vector. To clarify our procedure, an example is given: If only 5 % of the coefficients are used in the first test, and in a second test 10 % of the coefficients are used, then the 10 % test also includes all coefficients of the 5 % test. We created ten different sampling patterns and repeated all experiments for the CS-based system matrix reconstruction ten times. Inside the system matrix reconstruction, no assumptions on symmetric structures were used, like in [9]. To make a fair comparison, it is necessary that all system matrices are reconstructed in the same manner. However, for all trajectories, the system matrices show highly symmetric structures, and we expect that the symmetries can be proofed by similar techniques as in [8]. For all system matrices, we observe only even- and odd-symmetric system function components along the x- and y-direction inside the spatial domain. Because the results in [7–9, 12, 13] show that it is preferable to use a transform for compression that exploits the symmetries, we decided to use the two-dimensional DCT-II for this purpose.

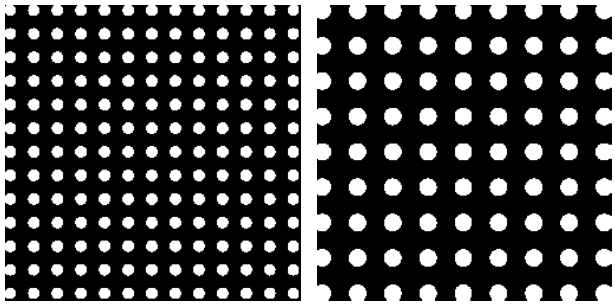

(a) (b)

Figure 2: The two test phantoms. Here, the areas with particle concentration equal to one are shown in white. Black is used for areas without particles. In the phantom (a), a circle has a diameter of 2 mm. In the phantom (b), a circle has a diameter of 3 mm.

Inside the FISTA reconstruction, all system function components were separately reconstructed. Each system function component was additionally split into real and imaginary parts for the reconstruction. The ℓ_1-constraint parameter was handcrafted as $\lambda = 10^{-8}$ inside the reconstruction and the reconstruction was run until the change of the coefficients between different iterations was lower than a threshold or the objective function did not change significantly anymore.

To show the efficiency of the reconstructed system matrices, the following reconstruction problem was solved for the resolution phantoms shown in Fig. 2:

$$\boldsymbol{c}^* = \underset{\boldsymbol{c}\in\mathbb{R}_+^{N_1\cdot N_2}}{\arg\min} \left\| \hat{\boldsymbol{S}}\boldsymbol{c} - \hat{\boldsymbol{u}} \right\|_2^2 + \mu\|\boldsymbol{c}\|_2^2. \tag{18}$$

The parameter μ was chosen for all trajectories handcrafted as $\mu = 10^{-9}$, so that visually best results over all trajectories were reached. To simplify the paper, we excluded the study of finding optimal μ's for all trajectories. Inside the reconstruction, no deletion or normalization of system function components was performed. The reconstruction was performed by the regularized Kaczmarz method with setting the negative and imaginary parts in $\boldsymbol{c}^l$ during each iteration l to zero [25]. Furthermore, we also performed the reconstruction with the FISTA algorithm by making use a proximity operator with respect to the nonnegativity constraint and the ℓ_2-regularization term [23, 26, 27].

10.18416/ijmpi.2017.1706005

VII. Results

The result section is subdivided into subsections to investigate different aspects of the CS-based system-matrix reconstruction. The first subsection investigates the question of the compressibility of the different system matrices by the DCT-II. The second subsection investigates the mutual coherence of sampling patterns and the influence on the image reconstruction with the CS-based system matrices. Then we look at the spatial distribution of errors on CS-recovered system matrices. Finally, the last subsection investigates the image reconstruction performance of CS-based MPI system matrices for different FFP trajectories.

VII.I. Compressibility of the system-matrix coefficients

w

In this section, the compressibility of the different simulated system matrices will be investigated with help of the two-dimensional DCT-II as compressive orthogonal transform. It should be noted here that a systematic study of different other compressive transforms was not performed. However, the compressibility of the different system matrices is a necessary condition for compressed-sensing reconstruction techniques to work. To demonstrate that the DCT-II is a suitable compressive transform for all system matrices, two different measures obtained from [28] will be introduced. In [28], different commonly used sparsity measures were investigated with regard to their suitability under different manipulations of the coefficients. The two sparsity measures for $\boldsymbol{x} \in \mathbb{R}^N$ used here are

$$\ell_{0,\epsilon}^{\text{norm}}(\boldsymbol{x}) = \frac{\#\left(\left\{i \in \{0,1,\ldots,N-1\} \;\middle|\; |x_i| > \epsilon\right\}\right)}{N} \quad \text{and} \quad \frac{\ell_1}{\ell_2}(\boldsymbol{x}) = \frac{\|\boldsymbol{x}\|_1}{\|\boldsymbol{x}\|_2}, \tag{19}$$

where $\#(\,\cdot\,)$ denotes the cardinality of a set. Both measures decrease with increasing sparsity. The variable ϵ for $\ell_{0,\epsilon}^{\text{norm}}(\,\cdot\,)$ is chosen in such a way that 99 % of the energy is recovered from the original $\boldsymbol{x}$. In Tab. 2 the global compression performances are shown. By global compression performance we mean that the two measures are evaluated for each vectorized system matrix before and after the application of the 2D DCT-II to the spatial dimension. It is clearly visible that system matrices can be highly compressed by the DCT-II. Here, according to both measures, the system matrices for an MPI scanner with the FFP traveling along a Lissajous trajectory have the best compression performance. The Cartesian FFP trajectory system matrix shows a better compression ratio for one receive channel than for the other. Both completely symmetric FFP trajectories (flower and radial) have the same compression performance for both receive-channel system matrices, which is due to the orthogonal setting of the receive coils. It should be noted that these symmetries might be useful for further compression. In a second test, the local compression ratio for each system function component k was investigated. Therefore, a plot of the ratios $\ell_{0,\epsilon}^{\text{norm}}(\tilde{\boldsymbol{s}}_{\ell,k})/\ell_{0,\epsilon}^{\text{norm}}(\hat{\boldsymbol{s}}_{\ell,k})$ of the compressed $\tilde{\boldsymbol{s}}_{\ell,k}$ to the uncompressed $\hat{\boldsymbol{s}}_{\ell,k}$ system function components is presented. Fig. 3 shows that the system matrices transformed by the 2D DCT-II are generally more sparse than the untransformed ones. For some compressed system function components, the number of remaining coefficients is by a factor of 10^{-4} smaller than for the uncompressed system function components. While there are several system function components with a low compression ratio of $\ell_{0,\epsilon}^{\text{norm}}(\tilde{\boldsymbol{s}}_{\ell,k})/\ell_{0,\epsilon}^{\text{norm}}(\hat{\boldsymbol{s}}_{\ell,k})$ being approximately equal to one, the ratio does not become higher than one, which is a good indicator for system function components with a low signal-to-noise ratio. It should be noted that a low compression ratio in this test can have two reasons. The first reason is that a system function component has a low signal-to-noise ratio due to the corruption with simulated white Gaussian noise, and white noise cannot be compressed. The second reason is a high number of spatial frequencies inside the system function component $\hat{\boldsymbol{s}}_{\ell,k}$, as for such structures, the 2D DCT-II cannot be a compressive transform. To this point, it has been shown that all system matrices are highly compressible by the 2D DCT-II and compressed-sensing based reconstruction of several system function components should be possible from a partial number of calibration scans.

VII.II. Mutual Coherence

For the evaluation of the ten different sampling patterns, where the coordinates are taken from a uniform distribution, the mutual coherence is calculated according to Eq. (12). Specially, for the CS-based recovery of the system matrix, the measurement matrix $\boldsymbol{A}$ is a composition of the undersampling matrix $\boldsymbol{U}$ and the two-dimensional DCT-II matrix. The calculation of $\mu(\boldsymbol{A})$ is quite time consuming for large M and N. Obviously, the number of scalar products $\left|\left\langle \boldsymbol{a}_i, \boldsymbol{a}_j \right\rangle\right|$ to be calculated is given by $(N^2-N)/2$, because $\left|\left\langle \boldsymbol{a}_j, \boldsymbol{a}_i \right\rangle\right| = \left|\left\langle \boldsymbol{a}_i, \boldsymbol{a}_j \right\rangle\right|$. For each scalar product, M multiplications and $M-1$ additions have to be performed. Since multiplication is the computationally more challenging calculation, only the multiplications are counted in the following. Overall, $M(N^2-N)/2$ multiplications have to be performed, and the computational complexity is in $\mathcal{O}(MN^2)$. Within the parameter ranges in this article, $M(250^4-250^2)/2 = 1953093750 \cdot M$ multiplications have to be performed. Even if M is small, the process of calculating the mutual coherence is highly time consuming and, in general, not practical for large scenarios. Due to this reason, the mutual coherence is only determined for "high" under-

10.18416/ijmpi.2017.1706005

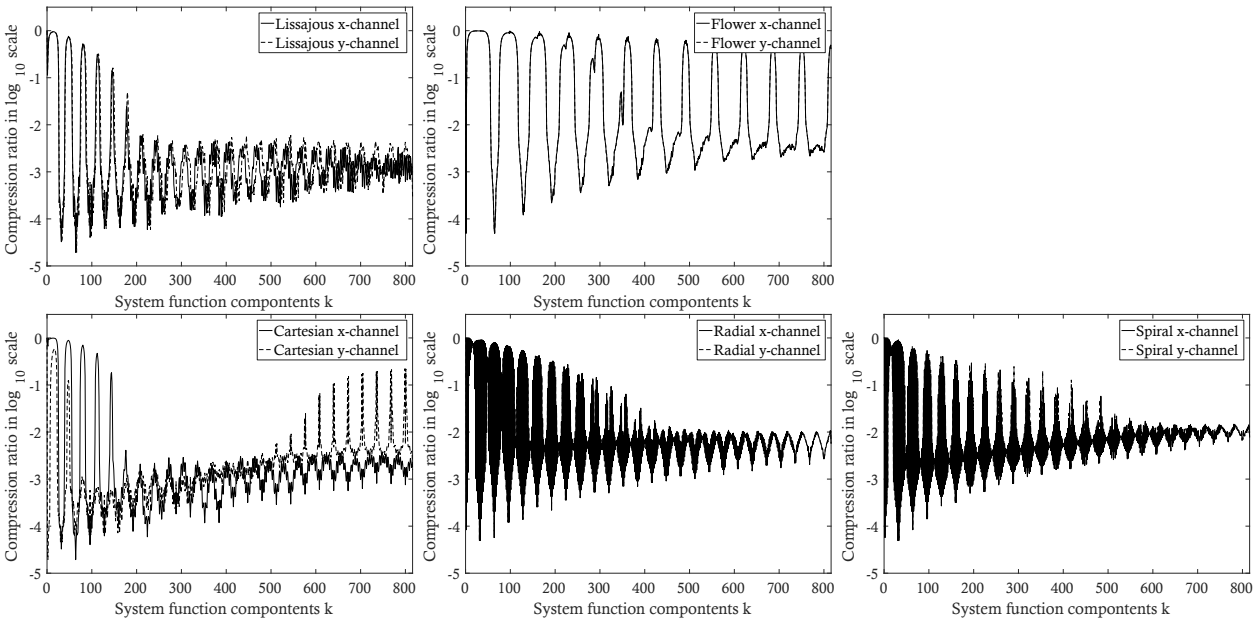

Figure 3: The compression ratio of $\ell_{0,\epsilon}^{\text{norm}}(\tilde{\boldsymbol{s}}_{\ell,k})/\ell_{0,\epsilon}^{\text{norm}}(\hat{\boldsymbol{s}}_{\ell,k})$ as function of the system function components k for both receive channels of the system matrices from an MPI scanner with different FFP trajectories. Here $\tilde{\boldsymbol{s}}_{\ell,k}$ denotes the DCT-II transformed system matrices, whereas $\hat{\boldsymbol{s}}_{\ell,k}$ denotes the uncompressed system matrix. The plot is shown in logarithmic scale to the base 10.

Table 2: Global compression measure (mes) calculated for simulated system matrices of an MPI scanner with the FFP traveling along different trajectories for both receive channels (chan). The measure $\ell_{0,\epsilon}^{\text{norm}}$ is given in percentage of necessary coefficients to cover 99 % of the energy. The measure $\frac{\ell_1}{\ell_2}$ is round to integer numbers.

chan	mes	Lissajous		Flower		Cartesian		Radial		Spiral	
		org	DCT-II	org	DCT-II	org	DCT-II	org	DCT-II	org	DCT-II
x	$\ell_{0,\epsilon}^{\text{norm}}$	37.74	0.0084	20.90	0.0238	44.50	0.0112	28.11	0.0321	31.67	0.0488
	$\frac{\ell_1}{\ell_2}$	2874	106	2280	112	2939	114	2471	146	2577	170
y	$\ell_{0,\epsilon}^{\text{norm}}$	34.13	0.0079	20.90	0.0238	65.28	0.0384	28.11	0.0321	31.75	0.0489
	$\frac{\ell_1}{\ell_2}$	2797	104	2280	122	4285	227	2471	146	2579	169

sampling factors (i.e., small M), so that only $\{2, 2.5, \ldots, 5\}$ percent of the original spatial coefficients are sampled. In Tab. 3 it is observable that all patterns are more or less on the same level in terms of mutual coherence. Additionally, the so called Welch bound as lower limit of the mutual coherence is given for each sampling ratio. The Welch bound is computed as

$$\mu(\boldsymbol{A}) \geq \sqrt{\frac{N-M}{M(N-1)}}. \tag{20}$$

The upper bound is given by $\mu(\boldsymbol{A}) \leq 1$.

With help of a first phantom reconstruction test, the image reconstruction with the CS-based system matrices for the sampling patterns will be compared with the mutual coherence given in Tab. 3. Exemplarily, here the sampling pattern 5 and the sampling pattern 4 will be compared. For the image reconstruction test, the 3 mm phantom from Fig. 2 (b) is taken. The results are shown in Fig. 4. We evaluate the reconstruction by the normalized root mean square error, which is given by

$$\text{NRMSE} = \frac{\|\boldsymbol{c}^* - \boldsymbol{c}_{\text{org}}\|_2}{\sqrt{N_1 N_2}\big(\max(\boldsymbol{c}_{\text{org}}) - \min(\boldsymbol{c}_{\text{org}})\big)}, \tag{21}$$

where $\boldsymbol{c}^*$ denotes the reconstructed particle distribution, $\boldsymbol{c}_{\text{org}}$ is the original particle distribution, and $\max(\boldsymbol{c}_{\text{org}})$ and $\min(\boldsymbol{c}_{\text{org}})$ are the highest and smallest values in $\boldsymbol{c}_{\text{org}}$, respectively. It is recognizable that for all FFP trajectories, sampling pattern 4 (solid lines) outperforms sampling pattern 5 (dashed lines) when the system matrices are obtained within a CS framework. By the mutual coherence as measure (see Tab. 3) a different outcome would be expected, because pattern 5 has most often a smaller mutual coherence than pattern 4. It becomes clear that the mutual coherence can only be understood as a rough indication of possible performance, not as a strict performance measure. A source of the problem could be the

Table 3: The mutual coherence calculated by (12) for ten sampling patterns uniformly sampled form all possible pixels inside the FOV. The number of sampled position (Pos.) is given in %. Additionally, the Welch Bound (WB) is given as lower boundary.

Pos.	Sampling pattern										
in %	1	2	3	4	5	6	7	8	9	10	WB
5.0	0.1120	0.1153	0.1114	0.1165	0.1136	0.1207	0.1157	0.1132	0.1132	**0.1103**	0.0174
4.5	0.1163	0.1173	0.1189	0.1184	0.1199	0.1235	0.1183	0.1163	0.1224	**0.1160**	0.0184
4.0	0.1305	0.1247	0.1286	**0.1217**	0.1254	0.1236	0.1292	0.1259	0.1330	0.1293	0.0196
3.5	0.1360	0.1370	0.1374	0.1450	**0.1298**	0.1339	0.1339	0.1317	0.1340	0.1357	0.0210
3.0	0.1557	0.1492	0.1537	0.1497	0.1463	0.1469	**0.1374**	0.1494	0.1502	0.1465	0.0227
2.5	0.1633	0.1611	0.1716	0.1624	0.1573	0.1610	**0.1506**	0.1545	0.1600	0.1593	0.0250
2.0	**0.1745**	0.1815	0.1870	0.1817	0.1781	0.1946	0.1808	0.1830	0.1833	0.1797	0.0280

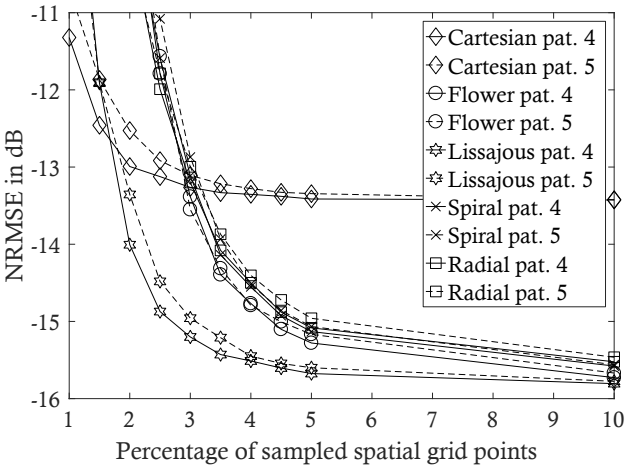

Figure 4: An example of an image reconstruction of the 3 mm phantom with CS-based system matrices for two different sampling patterns. The pattern 5 (dashed line) has mostly a lower mutual coherence than pattern 4 (solid line).

usage of the CS-based system matrices for estimation of the particle distribution, and in the moment this is not covered inside the CS-based framework.

When comparing Tab. 2 and Fig. 4, one can see that a larger compression ratio generally corresponds to a better reconstruction performance. However, establishing an exact numerical relationship between the compression ratio and the reconstruction error is quite difficult, because not only the trajectory and the sparsifying transform, but also the sparsity parameter λ influence the result.

VII.III. Spatial distribution of error on system matrices

To validate the spatial distributions of the reconstruction error on the CS-based system functions, we consider the absolute spatial error given by

$$\mathrm{ASE}(u,v) = \sqrt{\sum_{\ell=1}^{2}\sum_{k=0}^{K-1}\left|\hat{s}_{\ell,k}^{\mathrm{org}}(u,v) - \hat{s}_{\ell,k}^{\mathrm{CS}}(u,v)\right|^2} \tag{22}$$

with $\hat{s}_{\ell,k}^{\mathrm{org}}(u,v)$ being the original system function component without any compression or modification from a full calibration scan in each pixel and $\hat{s}_{\ell,k}^{\mathrm{CS}}(u,v)$ being the CS-based system function component. For each of the trajectories and ten different randomly generated sampling patterns, the mean ASE (MASE) was calculated. To enable a comparison between the spatial error distributions and the spatial sensitivities, also the sensitivity profiles

$$\mathrm{SP}(u,v) = \sum_{\ell=1}^{2}\sum_{k=0}^{K-1}\left|\hat{s}_{\ell,k}^{\mathrm{org}}(u,v)\right|^2 \tag{23}$$

have been computed. In Fig. 5, the top row shows the sensitivity profiles (SP) for the different trajectories. The middle row shows the MASE for CS-based system matrices derived from only 5% of the full number of calibration scans, whereas the lower row shows the MASE for CS-based system matrices recovered from only 2 % of a full calibration scan. The CS-based system matrices for trajectories with rectangular envelopes become worse firstly in the border regions of the FOV, where the FFP travels slow and the spatial sensitivity is low. In addition, for the CS-based system matrix for an MPI scanner with a Cartesian FFP trajectory and 2 % of a full scan, an increasing MASE related to the distance of the FFP trajectory can be observed in the center. The CS-based system matrix from the flower and radial trajectories have a lower MASE in the FOV than the CS-based system matrix from the spiral trajectory. However, both show a high-error spot directly in the center of the FOV. For the CS-based system matrix from the flower trajectory, the border region has a smaller mean absolute error than the one from the radial trajectory. The MASE of the CS-based system matrix from a spiral FFP-trajectory shows concentric higher-error regions around the center and very large errors along the boundaries.

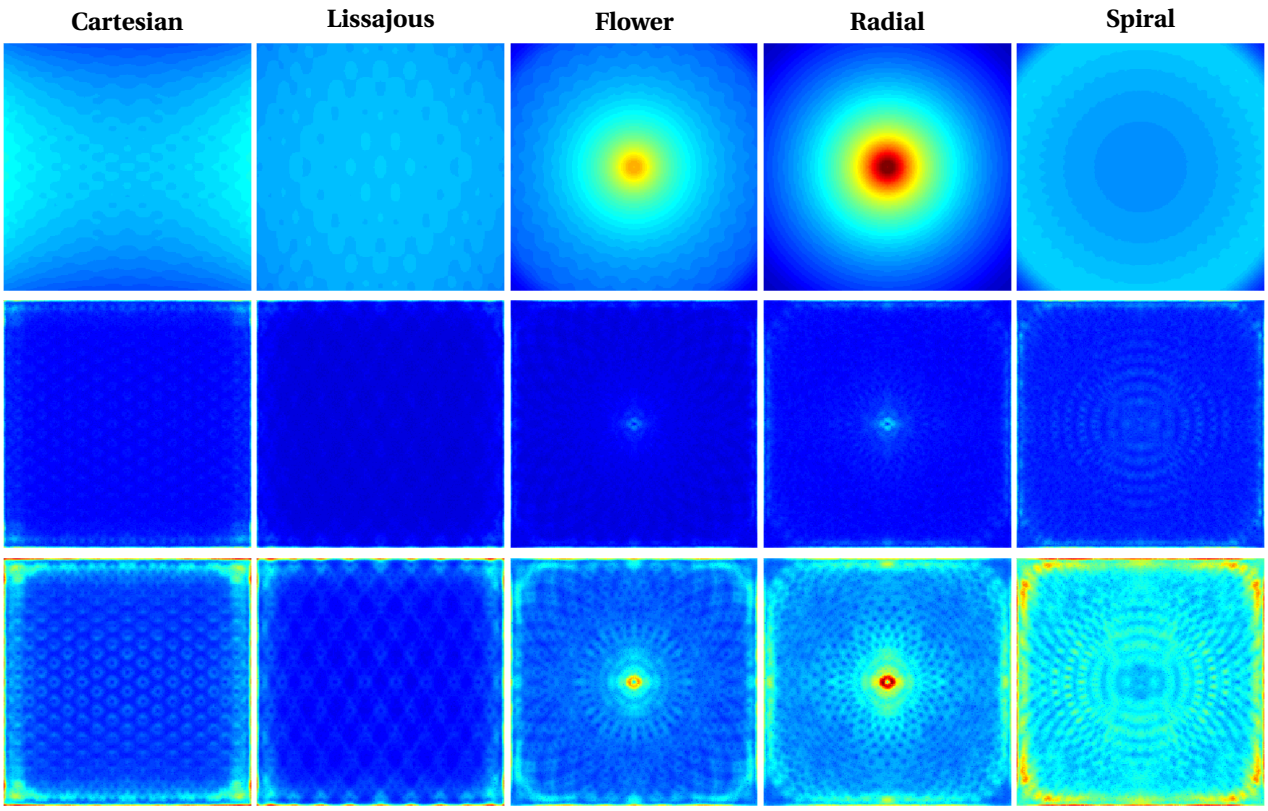

Figure 5: Sensitivity profiles for different trajectories and the corresponding MASE results for the CS-based system matrices as heat map (blue=small value / red=high value). The top row shows the spatial energy distribution inside the system matrices from full calibration scans (i.e., the sensitivity profiles). The middle row shows the MASE for only 5 % of calibrations scans. The bottom row shows the MASE for only 2 % of calibrations scans. The heat maps of the spatial energy distributions are scaled between the highest spatial energy component over all fully scanned system matrices. For the middle and bottom row, the full-calibration-scan system-matrix coefficients were normalized to have a unit Frobenius norm, where, in a first step, both receive channels were merged into one system matrix. The heat-map color is scaled between 0 and the highest spatial error over all trajectories from the system matrix reconstruction from only 2 % of calibration scans.

The observations on the spatial error distributions for Cartesian and Lissajous trajectories give rise to the assumption that the travel velocity of the FFP is an important parameter that governs the absolute error and determines in which region the largest error occurs in CS-based system matrices derived under uniform random sampling. For the spiral trajectory, it is most obvious that the distance of several pixels to the trajectory is a second important parameter. For the flower and radial trajectories, a higher error level occurs in a small region around the center of the FOV. With these trajectories, the center is crossed by the FFP from all directions, resulting in a particularly high sensitivity for this point. However, this rapid change of sensitivity toward the center could be occasionally missed by uniform random sampling. Moreover, the rapid change cannot be well represented by the DCT-II with only a few coefficients. Thus, the combination of low-density sampling and the inability of the sparsifying transform to properly approximate the system function components with very few coefficients seem to be another cause of error. To illustrate this more, Fig. 6 shows two examples of the obtained error distributions. The left image corresponds to a poor reconstruction of the center, whereas the right image is an example of a good reconstruction. In the lower detail plot it is visible that the configuration of the sampled points (dark blue) around the center is the reason for the poor reconstruction, because the center is not covered by the sampling points. In the right image, the sampling points are distributed closer to the center of the FOV, and a better reconstruction of the CS-based system matrix becomes possible. Thus, for such trajectories, it seems appropriate to adapt the sampling density to the spatial variation of the sensitivity. However, a full optimization of the sampling densities for all possible trajectories is out of the scope of this paper and will be addressed in future work.

VII.IV. Image reconstruction

In Fig. 7, we show the reconstruction results for the phantom in Fig. 2 (a) with a circle diameter of 2 mm for dif-

10.18416/ijmpi.2017.1706005

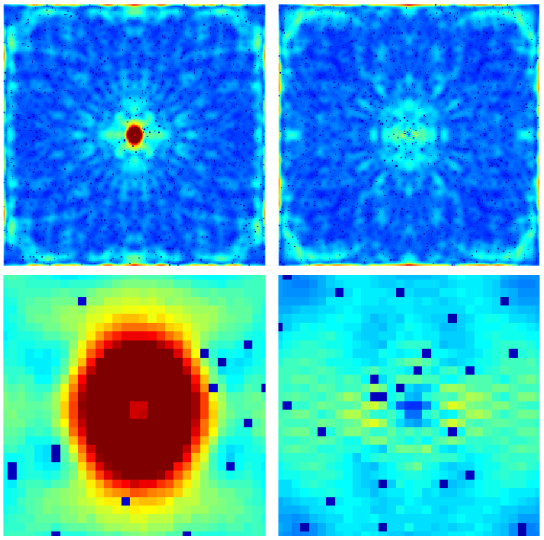

Figure 6: The absolute spatial error of the CS-based system matrix of an MPI scanner with a FFP that travels along the flower trajectory for two different sampling patterns, when only 2 % of calibration scans are performed. On the left, the result for sampling pattern 1, and on the right, the sampling pattern 7 is shown. The upper plot shows the absolute spatial error over the whole FOV, whereas the lower plot shows a detailed zoom of the center. The dark blue points in the lower plot correspond to the sampled spatial positions.

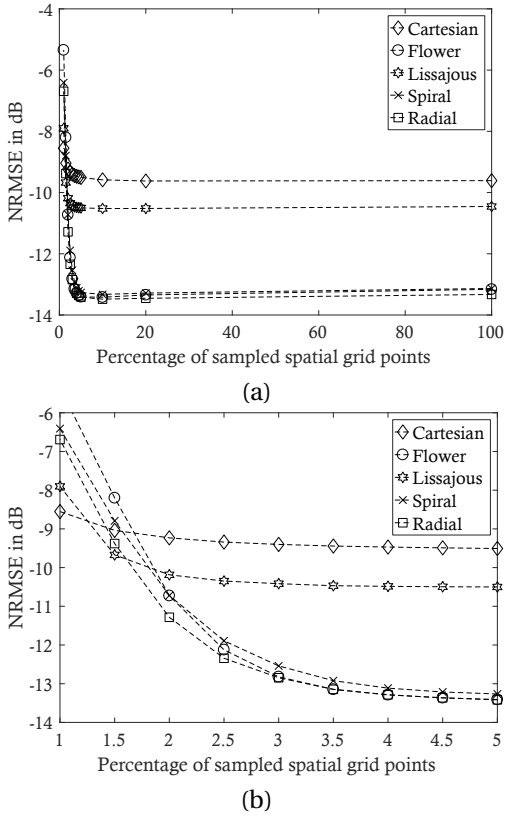

Figure 7: The mean over ten trials of the NRMSE for the reconstructed phantom in Fig. 2 (a) as function of the percentage of measured spatial grid points inside the calibration scan. One trial corresponds to the reconstruction from one random sampling pattern. The results are presented for five different trajectories. The upper plot shows the interval from 0 % to 100 %. The lower plot shows the interval from 1 % to 5 % in detail.

ferent trajectory choices. This experiment has been repeated 10 times with different randomly generated spatial sampling patterns and the mean over all trials was calculated. The standard deviation of the obtained RMSE-values turned out to be not more than one-tenth of the RMSE in the worst-case scenario. However, it could be observed that with a higher degree of undersampling the standard deviation increased. In Fig. 7 (a), we observe that the reconstruction with help of the partially measured system matrix works well for all trajectories when at least 5 % of coefficients are retained. In this case, the reconstruction results seem to depend only on the resolution properties of the trajectory choices. We observe that the trajectories with a circular envelope (flower, radial, spiral) offer similar performance with respect to the NRMSE. For the trajectories with a rectangular envelope the Lissajous trajectory based system matrix yields about 1 dB better performance than the Cartesian trajectory based system matrix. The difference between the trajectories with a circular and rectangular envelope for the CS-based system matrices is about 3 dB. To see what happens when less than 5 % of coefficients are observed and the CS-based system matrices start to fail to reconstruct the particle distribution, we plot in Fig. 7 (b) the NRMSE for the interval from 1 % to 5 % of remaining coefficients. Here we can observe that the trajectories with rectangular envelope seem to be more robust against a higher degree of information loss on the system matrix than the circular variants. Comparing the trajectories with a rectangular envelope among one another, it becomes obvious that the Cartesian trajectory is more robust than the Lissajous trajectory to the loss of information in the system matrix.

Because the spatial resolution seems to be the limiting factor for the Lissajous and Cartesian trajectories, the previous experiment was repeated for the phantom in Fig. 2 (b), where the diameter of one circle filled with particles is now 3 mm. The results of this experiment are shown in Fig. 8. In Fig. 8 (a) it can been observed that the flower, Lissajous, spiral, and radial trajectories have similar resolution performance, whereas the Cartesian one is about 2 dB lower in the reconstruction result. For this phantom a small loss of reconstruction performance starts at about 90 % of undersampling. Therefore, in Fig. 8 (b), the interval up to 10 % remaining coefficients is shown. As for the first phantom, it can be observed that the rectangular-envelope CS-based system matrices seem to be more robust against a higher loss of information through the CS-based reconstruction of the system

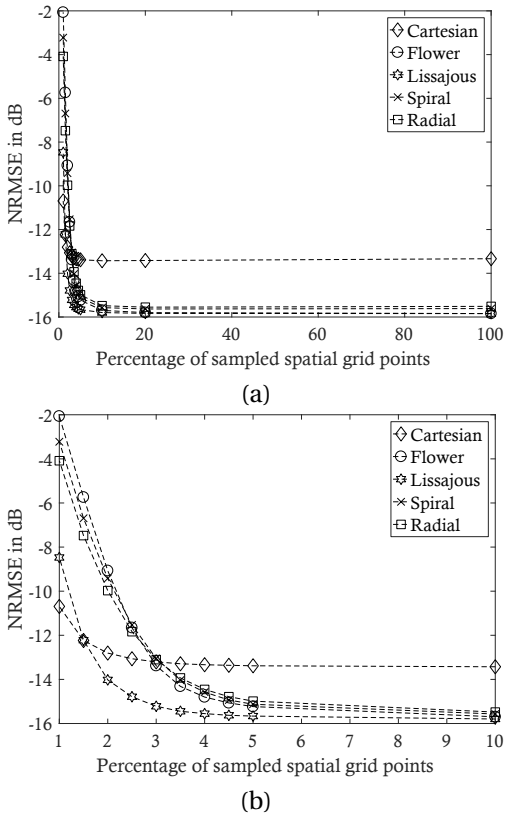

Figure 8: The mean over ten trials of the NRMSE for the reconstructed phantom in Fig. 2 (b) as function of the percentage of measured spatial grid points inside the calibration scan. One trial corresponds to reconstruction from one randomly selected sampling pattern. The results are presented for five different trajectories. The upper plot shows the interval from 0 % to 100 %. The lower plot shows the interval from 1 % to 10 % in detail.

matrix than the ones with circular envelope. Additionally, the Cartesian trajectory is the most robust trajectory against a high level of undersampling.

The reconstructions from CS-based system matrices for MPI scanners with a spiral and radial trajectory show no significant differences in the performance in the highly undersampled case. Interestingly, in the extremely undersampled case, the flower trajectory yields worse reconstruction results than the rest of the trajectories. Quite obviously and not surprisingly, the temporal acceleration frequencies f_1 and f_2 have a significant effect on the robustness of the compressed sensing based approach. The reason is that f_2 in the second group in Tab. 1 (Cartesian, radial, spiral) is by a magnitude smaller than in the first group (Lissajous, flower). The second important contribution seems to be the rotation parameter in radial, spiral, and flower against the other two trajectories (Lissajous, Cartesian).

In the following, we investigate directly the reconstructed particle distributions for the phantoms and differently strong undersampled FOVs. In Fig. 9, the resolution phantom with a circle diameter of 2 mm is shown. Because the trajectories with rectangular envelopes (Cartesian, Lissajous) were not really able to reconstruct this phantom, they will be excluded from the following discussion. We obverse that the trajectories with circular envelopes offer a sufficiently high spatial resolution for the reconstruction of this phantom. For 5 % of sampled spatial points, the visual impression of the phantom reconstruction is similar to the fully sampled system matrices. Some small differences can be observed around the center axis in the image reconstructed with the CS-based system matrix from an MPI scanner with a radial and spiral trajectory, whereas the reconstruction from a CS-based system matrix with an FFP that travels along a flower trajectory does not show significant differences. However, if only 2 % of the grid points of the FOV are measured, peak-like noise of salt-and-pepper type appears in the images obtained from trajectories with circular envelopes. This noise seems to be related to nearly singular values inside the CS-based system matrix for some single pixels. The flower trajectory based system matrix equally distributes the noise over the whole reconstruction. The radial trajectory has a tendency to result in most noise at the borders of the FOV and in a region near to the center, the spiral case shows most noise in the center and around the center axes.

Because the system matrices for an MPI scanner with an FFP that travels along a Lissajous or Cartesian trajectory did not allow for a proper reconstruction of the phantom in Fig. 9, we also investigated the reconstruction of a different phantom with a circle diameter of 3 mm. The results are shown in Fig. 10. Here, the reconstruction from a Cartesian trajectory still fails in the center of the image, but the system matrices for an MPI scanner with the FFP traveling along a Lissajous trajectory work sufficiently. For the image reconstruction with a CS-based system matrix obtained from only 5 % of sampled pixels the FFP trajectories with rectangular envelopes show no difference, whereas the ones with circular envelopes result in slight deformations of the circles. When only 2 % of spatial points are sampled and the system matrices are reconstructed in a CS-based framework, all image reconstructions of the second phantom include salt-and-pepper like noise. For the Cartesian trajectory only in the border regions the salt-and-pepper like noise appears, whereas in the center of the image, the included noise looks more Gaussian like. For the Lissajous trajectory a similar behavior can be observed. The flower trajectory distributes the salt-and-pepper like noise over the whole FOV. For the radial trajectory, similar observations as for the flower trajectory can be made, however the salt-and-pepper like noise is more observable in the border regions and directly in a small area around the center of the FOV, where the trajectory is crossing from all directions. For the radial trajectory the noise level seems

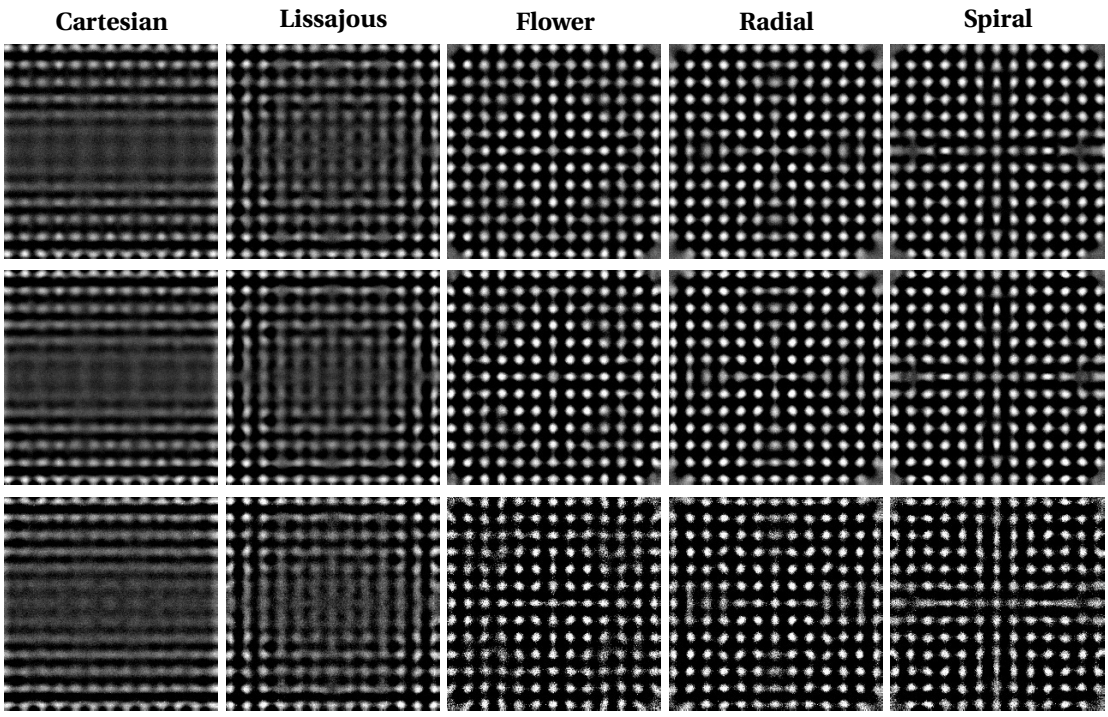

Figure 9: The reconstruction results of the particle phantom in Fig. 2 (a) for different trajectories shown for values in the interval $[0, 1]$. The top row shows the reconstruction results for the system matrices with full calibration scans. The middle row shows the reconstruction results from CS-based system matrices obtained from 5 % of calibration scans. The bottom row shows results from CS-based system matrices obtained from 2 % of calibration scans. Note that some individual errors may be larger than the figures suggest, because the estimated particle distributions had to be clipped for visualization in order to fit the given grayscale.

overall lower than for the flower trajectory. As with the previous phantom, for the reconstruction from the spiral trajectory we have an increased noise level in the center and along the axes of the image.

VIII. Conclusions

We studied in this paper different magnetic particle imaging trajectories for system matrices obtained via a compressed sensing framework. Within the simulation model, our results show that all trajectories offer highly compressible spatial structures, so that system matrices corresponding to all five trajectories can be recovered from only 5 % to 10 % of measured spatial positions without significant loss of quality for the reconstructed particle distribution. Additionally, we observed a correlation between the velocity of the FFP in the trajectory, the distance of pixels to the trajectory, and the reconstruction error of particle phantoms that occurs when using CS-based system matrices. A more complicated situation appears in the spatial center region of the system matrix for a scanner with radial or flower trajectory. Here the sampling pattern in the center has to be chosen more carefully than for the other trajectories. The results show that the Cartesian trajectory is the most stable choice if a very high level of undersampling is the goal. The Lissajous trajectory can be set between the Cartesian trajectory and the ones with circular envelope. The spatial resolution of the Lissajous trajectory is more limited than for trajectories with the circular envelope, but it is still better than for the Cartesian trajectory. In particular, it offers a higher stability to information loss than the trajectories with circular envelope. To make a decision within the group of trajectories with circular envelope is difficult. They all offer a higher spatial resolution than the two rectangular ones, but they have their individual pros and cons. Therefore, and because we only investigated uniform random spatial sampling, the question of which is the best trajectory for CS-based MPI still remains. Additionally, it should be noted here that the Lissajous and Cartesian trajectories are technically easier to realize than the circular ones. Also the step from the two-dimensional setting to the three-dimensional MPI is for some trajectories more challenging than for others. Our results will hopefully help to improve the sampling patterns for CS-based system matrix reconstruction. In an upcoming study, we will validate our simulation results with help of the hybrid system matrix approach.

10.18416/ijmpi.2017.1706005

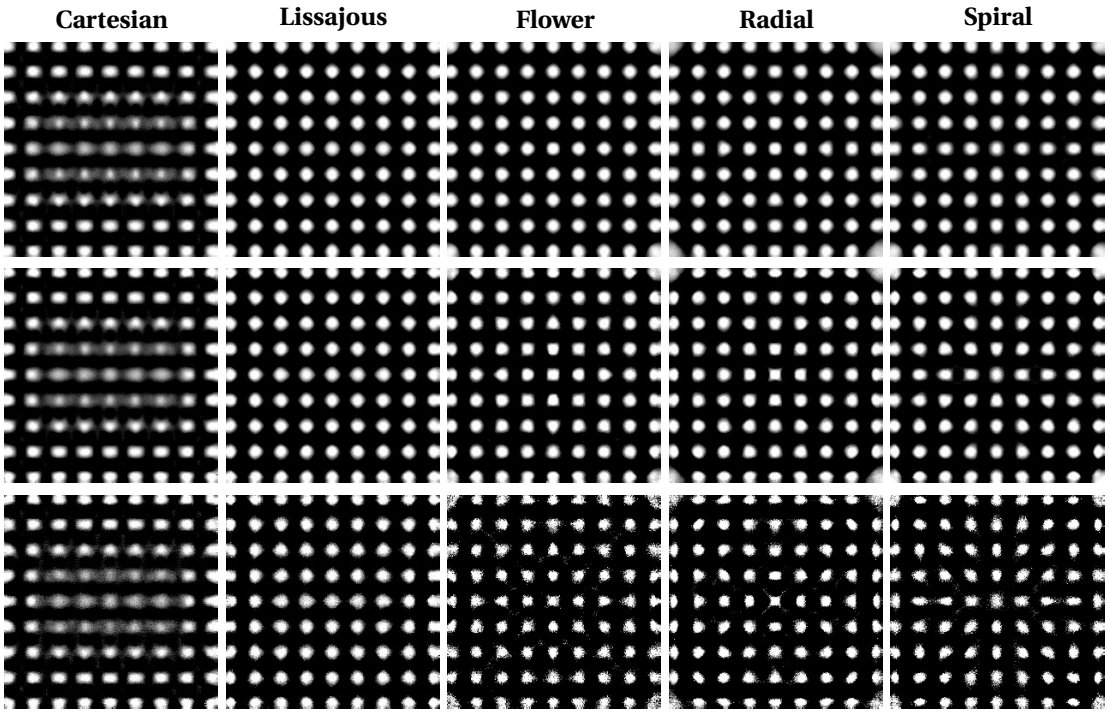

Figure 10: The reconstruction results of the particle phantom in Fig. 2 (b) for different trajectories shown for values in the interval $[0, 1]$. The top row shows the reconstruction results for the system matrices with full calibration scans. The middle row shows the reconstruction results from CS-based system matrices obtained from 5 % of calibration scans. The bottom row shows results from CS-based system matrices obtained from 2 % of calibration scans. Note that some individual errors may be larger than the figures suggest, because the estimated particle distributions had to be clipped for visualization in order to fit the given grayscale.

IX. Acknowledgments

This work was supported by the German Research Foundation under grant numbers ME 1170/7-1 and BU 1436/7-1.

References

[1] B. Gleich and J. Weizenecker. Tomographic imaging using the nonlinear response of magnetic particles. *Nature*, 435(7046):1214–1217, 2005. doi:10.1038/nature03808.

[2] T. Knopp and T. M. Buzug. *Magnetic Particle Imaging: An Introduction to Imaging Principles and Scanner Instrumentation*. Springer, Berlin/Heidelberg, 2012. doi:10.1007/978-3-642-04199-0.

[3] P. W. Goodwill and S. M. Conolly. Multidimensional X-Space Magnetic Particle Imaging. *IEEE Trans. Med. Imag.*, 30(9):1581–1590, 2011. doi:10.1109/TMI.2011.2125982.

[4] M. Grüttner, M. Graeser, S. Biederer, T. F. Sattel, H. Wojtczyk, W. Tenner, T. Knopp, B. Gleich, J. Borgert, and T. M. Buzug. 1D-image reconstruction for magnetic particle imaging using a hybrid system function. In *Nuclear Science Symposium and Medical Imaging Conference*, pages 2545–2548, 2011. doi:10.1109/NSSMIC.2011.6152687.

[5] M. Graeser, A. von Gladiss, P. Szwargulski, M. Ahlborg, T. Knopp, and T. M. Buzug. Reconstruction of Experimental 2D MPI Data using a Hybrid System Matrix. In *International Workshop on Magnetic Particle Imaging (IWMPI)*, page 130, 2016.

[6] D. Donoho. Compressed sensing. *IEEE Trans. Inf. Theory*, 52(4):1289–1306, 2006. doi:10.1109/tit.2006.871582.

[7] T. Knopp and A. Weber. Sparse Reconstruction of the Magnetic Particle Imaging System Matrix. *IEEE Trans. Med. Imag.*, 32(8):1473–1480, 2013. doi:10.1109/tmi.2013.2258029.

[8] A. Weber and T. Knopp. Symmetries of the 2D magnetic particle imaging system matrix. *Phys. Med. Biol.*, 60(10):4033–4044, 2015. doi:10.1088/0031-9155/60/10/4033.

[9] A. Weber and T. Knopp. Reconstruction of the Magnetic Particle Imaging System Matrix Using Symmetries and Compressed Sensing. *Adv. Math. Phys.*, 2015:460496, 2015. doi:10.1155/2015/460496.

[10] M. Ahlborg. *Bildgebungskonzepte für Magnetic Particle Imaging: Bildgebungskonzepte und Rekonstruktionsansätze für große Bildgebungsvolumen bei Magnetic Particle Imaging*. Infinite Science Publishing, 2016.

[11] J. Rahmer, J. Weizenecker, B. Gleich, and J. Borgert. Signal encoding in magnetic particle imaging: properties of the system function. *BMC Medical Imaging*, 9(4), 2009. doi:10.1186/1471-2342-9-4.

[12] J. Lampe, C. Bassoy, J. Rahmer, J. Weizenecker, H. Voss, B. Gleich, and J. Borgert. Fast reconstruction in magnetic particle imaging. *Phys. Med. Biol.*, 57(4):1113–1134, 2012. doi:10.1088/0031-9155/57/4/1113.

[13] M. Maass, K. Bente, M. Ahlborg, H. Medimagh, H. Phan, T. M. Buzug, and A. Mertins. Optimized Compression of MPI System Matrices Using a Symmetry-Preserving Secondary Orthogonal Transform. *Intern. J. Magnetic Particle Imaging*, 2(1):1607002, 2016. doi:10.18416/ijmpi.2016.1607002.

[14] T. Knopp and A. Weber. Local System Matrix Compression for Efficient Reconstruction in Magnetic Particle Imaging. *Adv. Math. Phys.*, 2015(472818), 2015. doi:10.1155/2015/472818.

[15] E. Candès and T. Tao. Decoding by Linear Program-

ming. *IEEE Trans. Inf. Theory*, 51(12):4203–4215, 2005. doi:10.1109/TIT.2005.858979.

[16] S. Foucart and H. Rauhut. *A Mathematical Introduction to Compressive Sensing*. Birkhäuser, Basel, 2013. doi:10.1007/978-0-8176-4948-7.

[17] M. Elad and A. M. Bruckstein. A Generalized Uncertainty Principle and Sparse Representation in Pairs of Bases. *IEEE Trans. Inf. Theory*, 48(9):2558–2567, 2002. doi:10.1109/tit.2002.801410.

[18] D. Donoho and M. Elad. Optimally sparse representation in general (nonorthogonal) dictionaries via ℓ_1 minimization. *Proceedings of the National Academy of Sciences*, 100(5):2197–2202, 2003. doi:10.1073/pnas.0437847100.

[19] R. Gribonval and M. Nielsen. Sparse Representations in Unions of Bases. *IEEE Trans. Inf. Theory*, 49(12):3320–3325, 2003. doi:10.1109/TIT.2003.820031.

[20] I. Daubechies, M. Defrise, and C. De Mol. An Iterative Thresholding Algorithm for Linear Inverse Problems with a Sparsity Constraint. *Comm. Pure Appl. Math.*, 57(11):1413–1457, 2004. doi:10.1002/cpa.20042.

[21] J. M. Bioucas-Dias and M. A. Figueiredo. A New TwIST: Two-Step Iterative Shrinkage/Thresholding Algorithms for Image Restoration. *IEEE Trans. Image Process.*, 16(12):2992–3004, 2007. doi:10.1109/TIP.2007.909319.

[22] W. Yin, S. Osher, D. Goldfarb, and J. Darbon. Bregman Iterative Algorithms for ℓ_1-Minimization with Applications to Compressed Sensing. *SIAM J. Imaging Sci.*, 1(1):143–168, 2008. doi:10.1137/070703983.

[23] A. Beck and M. Teboulle. A Fast Iterative Shrinkage-Thresholding Algorithm for Linear Inverse Problems. *SIAM J. Imaging Sci.*, 2(1):183–202, 2009. doi:10.1137/080716542.

[24] J. Weizenecker, B. Gleich, and J. Borgert. A simulation study on the resolution and sensitivity of magnetic particle imaging. *Phys. Med. Biol.*, 52(21):6363–6374, 2007. doi:10.1088/0031-9155/52/21/001.

[25] T. Knopp, J. Rahmer, T. F. Sattel, S. Biederer, J. Weizenecker, B. Gleich, J. Borgert, and T. M. Buzug. Weighted iterative reconstruction for magnetic particle imaging. *Phys. Med. Biol.*, 55(6):1577–1589, 2010. doi:10.1088/0031-9155/55/6/003.

[26] P. L. Combettes and J.-C. Pesquet. Proximal splitting methods in signal processing. In *Fixed-Point Algorithms for Inverse Problems in Science and Engineering*, volume 49, pages 185–212. Springer, New York, 2011. doi:10.1007/978-1-4419-9569-8_10.

[27] N. Parikh and S. Boyd. Proximal Algorithms. *Found. Trends Opt.*, 1(3):127–239, 2014. doi:10.1561/2400000003.

[28] N. Hurley and S. Rickard. Comparing Measures of Sparsity. *IEEE Trans. Inf. Theory*, 55(10):4723–4741, 2009. doi:10.1109/TIT.2009.2027527.

